p47 phox Molecular Activation for Assembly of the Neutrophil NADPH Oxidase Complex

Julien Marcoux, Petr Man, Isabelle Petit-Härtlein, Corinne Vivès, Eric Forest, Franck Fieschi

THE JOURNAL OF BIOLOGICAL CHEMISTRY VOL. 285, NO. 37, pp. 28980–28990, September 10, 2010

p47^{phox} Molecular Activation for Assembly of the Neutrophil NADPH Oxidase Complex*[S]

Received for publication, April 30, 2010, and in revised form, June 28, 2010 Published, JBC Papers in Press, June 30, 2010, DOI 10.1074/jbc.M110.139824

Julien Marcoux[‡§¶‖], Petr Man[§¶‖‡‡], Isabelle Petit-Haertlein[‡¶‖], Corinne Vivès[‡¶‖], Eric Forest[§¶‖], and Franck Fieschi[‡¶‖1]**

From the [‡]Laboratoire des Protéines Membranaires and [§]Laboratoire de Spectrométrie de Masse des Protéines, Commissariat à l'Energie Atomique (CEA), Direction des Sciences du Vivant, Institut de Biologie Structurale (IBS), 41 rue Jules Horowitz, Grenoble, F-38027, France, [¶]CNRS, UMR 5075, F-38027 Grenoble, France, the [‖]Université Joseph Fourier, F-38041 Grenoble, France, the [**]Institute of Microbiology, Academy of Sciences of the Czech Republic, v.v.i., Videnska 1083, CZ-14220 Prague 4, Czech Republic, and the [‡‡]Department of Biochemistry, Faculty of Science, Charles University in Prague, Hlavova 8, CZ-12840 Prague 2, Czech Republic

The p47^{phox} cytosolic factor from neutrophilic NADPH oxidase has always been resistant to crystallogenesis trials due to its modular organization leading to relative flexibility. Hydrogen/deuterium exchange coupled to mass spectrometry was used to obtain structural information on the conformational mechanism that underlies p47^{phox} activation. We confirmed a relative opening of the protein with exposure of the SH3 Src loops that are known to bind p22^{phox} upon activation. A new surface was shown to be unmasked after activation, representing a potential autoinhibitory surface that may block the interaction of the PX domain with the membrane in the resting state. Within this surface, we identified 2 residues involved in the interaction with the PX domain. The double mutant R162A/D166A showed a higher affinity for specific phospholipids but none for the C-terminal part of p22^{phox}, reflecting an intermediate conformation between the autoinhibited and activated forms.

NADPH oxidases (Nox) and Dual oxidases (Duox) are multienzymatic complexes found in many cell types (1) that play a wide range of physiological roles (2). The seven different isoforms of these enzymatic complexes differ in their membrane redox components: Nox1 to Nox5, Duox1 and Duox2. Despite this molecular heterogeneity, they all share the common feature of reactive oxygen species production, which is either constitutive (Nox4) or inducible by cytosolic factors (Nox1, Nox2, and Nox3) or Ca^{2+} (Nox5, Duox1, and Duox2).

The neutrophilic isoform containing Nox2, formerly called gp91^{phox}, is often referred to as a specialized reactive oxygen species producer as its main role is to trigger the oxidative burst in neutrophilic phagosomes leading to the killing of phagocytized pathogens. Of course, this catalytic activity must be tightly regulated to avoid excessive reactive oxygen species production, leading to oxidation of macromolecules, DNA mutations, aging, and cell death. In contrast, a defect in NADPH oxidase activity results in chronic granulomatous disease, an inherited immunodeficiency characterized by an abnormal inflammatory response and recurrent bacterial and fungal infections (3). This tight regulation is enabled by a physical separation before activation between the membrane-related flavocytochrome b_{558} (heterodimer of Nox2 and p22^{phox}), a small G protein (Rac1 or Rac2), and the cytosolic factors p40^{phox}, p47^{phox}, and p67^{phox}. In the resting state, these modular proteins form a heterotrimeric complex based on different interactions between their conserved binding domains (4); p40^{phox} and p67^{phox} interact via their respective PB1 domains (5, 6), and the p47^{phox} proline-rich region binds the p67^{phox} C-terminal SH3 [2] domain (7).

The p47^{phox} subunit is a key component in the activation process. It contains an N-terminal phox homology domain (PX) and SH3 domains arranged in tandem and ends with a proline-rich region (see Fig. 1). In the whole NADPH oxidase assembly, it acts as a sensor of the activation signal through multiple phosphorylations on serines within its autoinhibitory region (AIR). The activated form of p47^{phox} drives the translocation of the other cytosolic factors for assembly onto flavocytochrome b_{558} through the following mechanisms. Upon activation, the PX and tandem SH3s domains promote assembly through interactions with phosphoinositides (8–12) and p22^{phox} C-terminal proline-rich region (13–15), respectively. To avoid any constitutive binding to the membrane and maintain the cytosolic location of p47^{phox}, the tandem SH3s and PX domains must be masked in the resting state. Two functional states of p47^{phox} had already been proposed, corresponding to both activated and autoinhibited conformations.

The first p47^{phox} autoinhibited model suggested an interaction between the tandem SH3s and some downstream residues (13), lately defined as the AIR. Since the original proposal, many studies have tried to decipher the relative organization of the different domains in the autoinhibited state. Concomitantly with this first interaction arose the hypothesis of another interaction between the PX and SH3B domains (9), which was widely accepted in the field (4, 7, 8, 16, 17). New insights into the molecular mechanism of inhibition were provided by the structure of the tandem SH3s interacting either with the AIR or with

* This work was supported by grants from the CEA and the Association pour la Recherche sur le Cancer.

[S] The on-line version of this article (available at http://www.jbc.org) contains supplemental Table S1 and Figs. S1–S4.

[1] To whom correspondence should be addressed: IBS, 41 rue Jules Horowitz, Grenoble F-38027, France. Tel.: 33-4-3878-91-77; Fax: 33-4-38-78-54-94; E-mail: franck.fieschi@ibs.fr.

[2] The abbreviations used are: SH3, Src homology 3; phox, phagocyte oxidase; AIR, autoinhibitory region; PX, Phox homology; SPR, surface plasmon resonance; DXMS, deuterium exchange coupled to mass spectrometry; PtdIns(3,4)P_2, phosphoinositol-3,4-biphosphate; POPC, 1-palmitoyl-2-oleyl-*sn*-glycero-3-phosphocholine; POPE, 1-palmitoyl-2-oleyl-*sn*-glycero-3-phosphoethanolamine; POPA, 1-palmitoyl-2-oleyl-*sn*-glycero-3-phosphate; Cter, C terminus; TM, transmembrane.

the C-terminal part of p22^{phox} (18). However, this result was totally incompatible with the interaction between the PX and SH3B domains because both interactions involve the same binding region in the tandem SH3s, as pointed out by several groups (17–20).

Recently, our group proposed a model for the global conformation of the entire p47^{phox} in the autoinhibited form, using small angle x-ray scattering (20). It allowed us to definitely discard the hypothesis of an interaction between the PX and SH3B domains. p47^{phox} small angle x-ray scattering envelopes suggested that the PX domain was located in the proximity of the first SH3 domain (SH3A), but it was not possible to conclude on whether the PX interacts directly with the SH3A or is maintained in close proximity by a structured linker. Moreover, this work has strengthened the AIR-tandem SH3s interaction hypothesis initially based on studies using p47^{phox} isolated modules. The AIR release from the tandem SH3s, occurring upon activation, has recently been confirmed by limited proteolysis coupled to mass spectrometry (21). Coupling between the AIR release and enhanced lipid binding affinity was shown, suggesting changes in PX domain accessibility. Deuterium exchange coupled to mass spectrometry (DXMS) performed on the entire proteins confirmed the conformational difference between the activated and autoinhibited state (21). However, conclusive data regarding the molecular mechanism of PX inhibition in the resting state and more precisely proofs of its involvement in any intramolecular interaction were still missing.

To get detailed insight into the structural changes of p47^{phox}, we extended our previous study and followed local deuteration kinetics in the individual parts of the protein in both states. We confirmed and more precisely described the exposure of the Src loops, from both SH3s, due to AIR release. Remarkably, for the first time, we identify a novel surface within the SH3A domain that is unmasked during activation. Using site-directed mutagenesis and the liposome binding assay, we confirm that this region is involved in the inhibition of the PX domain lipid binding properties.

This study contributes a final response to the question of the p47^{phox} autoinhibitory mechanism. The modular organization deciphered here, involving up to four regions, has never been reported, particularly regarding PX and SH3 domain interaction.

EXPERIMENTAL PROCEDURES

Materials—Glutathione-Sepharose high performance and SP Sepharose high performance columns were from GE Healthcare (Little Chalfont, Buckinghamshire, UK). Jupiter C18 column (50 × 1 mm; 5 μm, 300 Å) was from Phenomenex (Torrance, CA). C4 and C8 macro traps were from Michrom Bioresources, Inc. (Auburn, CA). Pepsin from porcine gastric mucosa and protease type XIII from *Aspergillus saitoi* were from Sigma-Aldrich. The following products were purchased from Avanti Polar Lipids (Alabaster, AL): 1-palmitoyl-2-oleyl-*sn*-glycero-3-phosphocholine (POPC), 1-palmitoyl-2-oleyl-*sn*-glycero-3-phosphoethanolamine (POPE), 1-palmitoyl-2-oleyl-*sn*-glycero-3-phosphate (POPA), and 1,2-dioleoyl-*sn*-glycero-3-(phosphoinositol-3,4-biphosphate) (PtdIns(3,4)P_2).

Protein Cloning, Expression, and Purification—cDNA encoding p47^{phox} residues 1–390 (p47^{phox}) or 1–342 (p47^{phox}ΔCter) and the cytosolic region of p22^{phox} (residues 132–195) were cloned into pGex-6P vectors, adding an N-terminal GST fusion tag (see Fig. 1). Mutations were introduced by PCR-mediated site-directed mutagenesis. Due to the genetic construct, the full-length p47^{phox} harbors 7 additional residues at the C terminus. All constructs were sequenced to confirm their identities.

p47^{phox}, p47^{phox}ΔCter, and GST-p22^{phox}Cter constructs were expressed in *Escherichia coli* BL21(DE3) and purified according to Durand *et al.* (20), with slight differences described hereafter. Lysis buffer for p47^{phox} purification included 1 mM EDTA, but we used 2 mM $MgCl_2$ supplemented with DNase and Complete EDTA-free protease inhibitor (Roche Diagnostics, Basel, Switzerland) for GST-p22^{phox}Cter purification. Buffers were set at pH 7.5 for p47^{phox} construct purification and at pH 7 (lysis buffer) and pH 8 (elution buffer) for GST-p22^{phox}Cter purification. GST cleavage gave rise to p47^{phox} encoding residues 1–342, which will be referred to as p47^{phox}ΔCter. GST-p22^{phox}Cter was not cleaved after glutathione-Sepharose elution but was reloaded twice on the same column to bind any residual GST and concentrated on an Amicon centrifugal device with a 10-kDa cutoff (Millipore, Billerica, MA).

GST used for surface plasmon resonance (SPR) experiments was obtained after GST-p47^{phox}ΔCter overnight cleavage with PreScission protease (GE Healthcare). It was recovered from SP Sepharose column flow-through and concentrated on an Amicon centrifugal device with a 10-kDa cutoff.

p47^{phox}tandem SH3s was also purified according to Durand *et al.* (20), with slight differences. The culture pellet was resuspended in 50 mM Tris, pH 7, 300 mM NaCl, 2 mM EDTA, 4 mM 1–4-dithiothreitol (DTT) in the presence of Complete protease inhibitor. After overnight digestion at 4 °C with PreScission protease, the cleaved protein was precipitated with 60% ammonium sulfate and purified using a Superdex 75 prep grade column (GE Healthcare). The p47^{phox}tandem SH3s was finally eluted as a dimer, and the fractions were pooled and concentrated to 2.5 mg/ml on an Amicon centrifugal device with a 10-kDa cutoff.

Surface Plasmon Resonance—SPR experiments were conducted using a Biacore 3000 instrument (Biacore AB, Paris, France) equipped with a CM4 sensor chip. The machine was primed with the running buffer (137 mM NaCl, 2.7 mM KCl, 8.1 mM Na_2HPO_4, 1.5 mM KH_2PO_4, pH 7.4, and 0.005% surfactant P20). p47^{phox} was diluted in the running buffer to the required concentrations reported in Fig. 2. Before immobilization, 70 μl of *N*-hydroxysuccinimide and 70 μl of 1-ethyl-3-(3-dimethylaminopropyl)-carbodiimide were first mixed, and 50 μl of the resulting mix were injected to prime the surface at 5 μl/min, as recommended by the manufacturer. Ten microliters of 78.2 nM GST-p22^{phox}Cter diluted in 4 mM sodium acetate, pH 5, were then immobilized at 5 μl/min, and 30 μl of ethanolamine were finally injected to saturate the surface. All runs were carried out at 20 °C and at a flow rate of 20 μl/min. After each injection, the surface was regenerated by a 10-μl injection of 10 mM NaOH at a flow rate of 20 μl/min. For each p47^{phox} injection (60 μl), a blank was run in parallel on a surface functionalized with 78.2

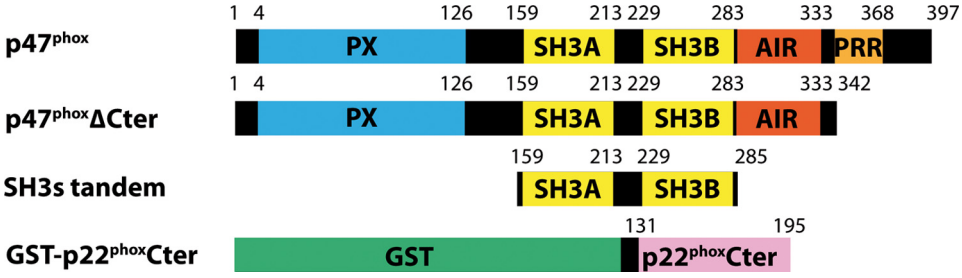

FIGURE 1. **Molecular constructs used in this study.** *PRR*, proline-rich region.

nM GST to subtract nonspecific binding. For the p47^{phox}ΔCter and p47^{phox}TM-ΔCter comparison, we carried out crossed scales to overcome the possible problems of surface degradation over time by alternating injections between p47^{phox}ΔCter, p47^{phox}TM-ΔCter, and p47^{phox}tandem SH3s. For point mutation analysis, crossed scales between p47^{phox}tandem SH3s and the mutants analyzed were carried out. For every third full-scale analysis, new CM4 surfaces were functionalized with both GST and GST-p22^{phox}Cter.

Multilamellar Vesicle Binding Assay—The *in vitro* semi-quantitative liposome binding assay was adapted from Ago *et al.* (8) with minor modifications. Liposomes were prepared by mixing POPC and POPE (50:50) for the control (MLV1) and POPC, POPE, POPA, and PtdIns(3,4)P_2 (45:45:5:5) for specific liposomes (MLV2). The mixture was then dried under nitrogen and resuspended to a concentration of 2 mM of total lipids in a binding buffer (20 mM Tris, pH 7.4, 100 mM NaCl, 1 mM DTT). After 2 h of incubation on ice, liposomes were obtained by vortexing. Proteins (5 μM) were incubated with liposomes (1 mM) for 15 min at 20 °C in 100 μl of binding buffer. Liposomes were collected by ultracentrifugation (1 h at 100,000 × *g* in an Airfuge rotor). Aliquots of bound (liposome pellet) and unbound p47^{phox} (supernatant) were taken for further analysis by 12% sodium dodecyl sulfate-polyacrylamide gel electrophoresis (SDS-PAGE). Coomassie Blue-stained gels were scanned and analyzed by densitometry. Three independent experiments were conducted.

H/D Exchange and Data Analysis—Deuteration of p47^{phox}ΔCter and p47^{phox}TM-ΔCter was initiated by a 20-fold dilution into a deuterated buffer (5 mM Hepes, pD 7.4, 1 mM EDTA, 2 mM DTT, and 200 mM NaCl). Aliquots (40 μl) were taken after 30 s, 1 min, 5 min, 10 min, 30 min, 1 h, 3 h, 5 h, 6 h, and 8 h for the local kinetics and 10 s, 30 s, 1 min, 5 min, 10 min, 30 min, and 1 h for the global kinetics. The exchange was done at 21 °C and was quenched by the addition of 5.6 μl of 50 mM HCl and rapid freezing in liquid nitrogen. Each sample was quickly thawed and digested on ice for 2 min with pepsin (enzyme/protein w/w ratio 1) or protease type XIII (enzyme/protein w/w ratio 12) before mass spectrometric analysis.

HPLC Separation—The digestion mixture was loaded on a peptide MacroTrap and desalted with 0.03% trifluoroacetic acid (TFA: solvent A) for 1 min at a flow rate of 400 μl/min. After that, peptides were eluted with a linear gradient (from 17 to 45% solvent B in 20 min, where solvent B was 95% acetonitrile, 0.03% TFA).

Mass Spectrometric Analysis—Peptide sequencing was performed using a quadrupole ion trap mass spectrometer (ESQUIRE 3000+, Bruker Daltonics) equipped with an electrospray source. For the MS/MS experiments, the three most intense ions from the preceding MS scan were fragmented. Tandem mass spectra were searched using Mascot, and the assignments were verified manually and by accurate mass measurements.

Accurate mass measurements and the analysis of the local kinetics of deuteration were done on a time-of-flight (TOF) mass spectrometer (6210, Agilent Technologies, Santa Clara, CA) equipped with an electrospray source. Data were processed with Analyst QS and MassHunter Qualitative Analysis, and the deconvolution and calculation of the average masses were carried out in Magtran (22). Deuteration percentages (%D) were calculated using Equation 1

$$\%D = [(m_{x\%} - m)/N] \times 100 \qquad \text{(Eq. 1)}$$

where m and $m_{x\%}$ represent the average molecular mass of non-deuterated and partially deuterated samples, respectively, and N represents the number of exchangeable amide protons. Two independent measurements were taken, and the data were averaged. Data were processed with the scripts available at the Laboratory of Molecular Structure Characterization (IMIC, Prague) MS Tools web page.

RESULTS

p47^{phox}TM-ΔCter Interacts with the C Terminus of p22^{phox}—To study the structural modifications occurring in p47^{phox} upon activation, we previously designed two recombinant forms corresponding to the autoinhibited and activated states (21). These p47^{phox} constructs are C-terminally truncated but still contain all the domains involved in the activation process (PX domain, tandem SH3s, and AIR) (Fig. 1). This C-terminal truncation (from residue 343) improves the homogeneity of the purified protein without affecting the structural integrity of the protein, as published previously (23).

To mimic serine phosphorylations occurring upon p47^{phox} activation, the corresponding serines 303, 304, and 328 were mutated into glutamic acid. We and others have shown that this triple mutant (p47^{phox}TM-ΔCter) presented an enhanced binding affinity for phosphoinositide lipids when compared with p47^{phox}ΔCter (8, 16, 21). In addition, structural analysis by deuterium exchange and limited proteolysis coupled to mass spectrometry also showed that this p47^{phox}TM-ΔCter presented a more open conformation, notably through release of the AIR (21). These previous characterizations supported the notion that p47^{phox}TM-ΔCter is a good mimic of the activated state. However, as a prerequisite to pursuing the detailed structural characterization of these two constructs, we needed to fully validate that the p47^{phox}TM-ΔCter is able to interact with p22^{phox}, as described earlier on the full-length p47^{phox} (18, 24).

SPR was used to quantify this interaction. CM4 surfaces were functionalized with a GST-p22^{phox}Cter construct (Fig. 1) or GST alone (negative control). Increasing p47^{phox}tandem SH3

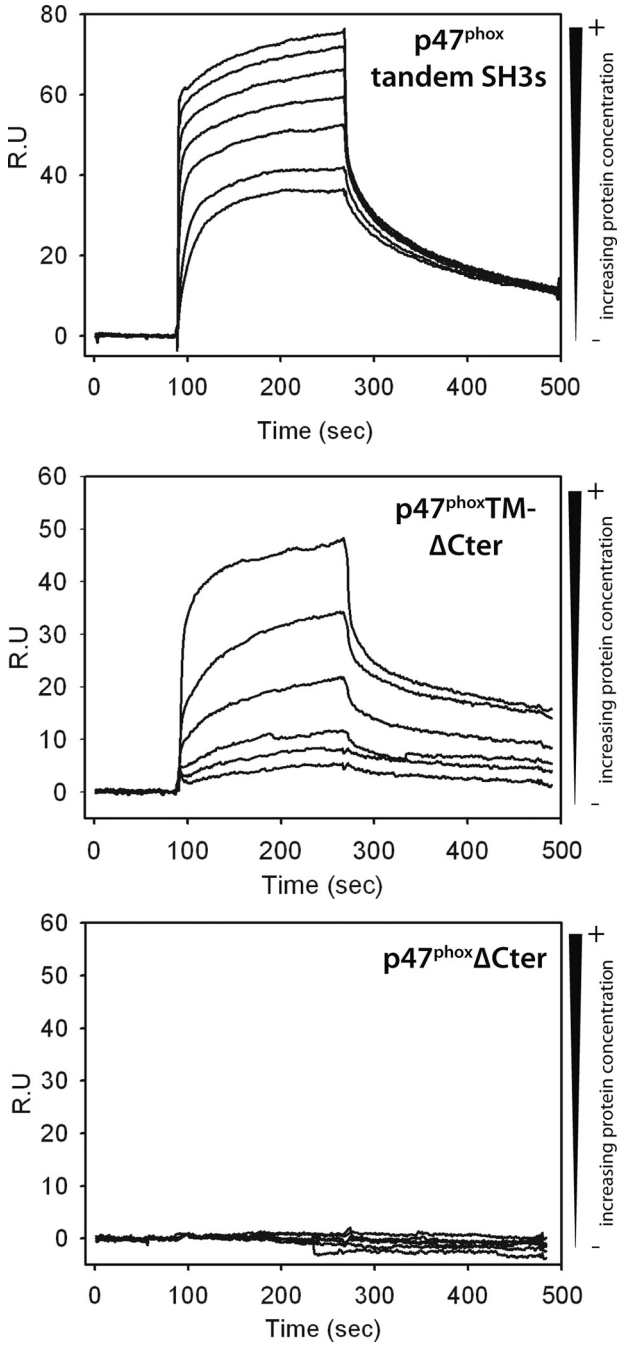

FIGURE 2. **Surface plasmon resonance results obtained for p47^{phox}tandem SH3s, p47^{phox}TM-ΔCter, and p47^{phox}ΔCter on CM4 chips functionalized with GST-p22^{phox}Cter.** Increasing concentrations (from 40 nM to 2.56 μM) of each construct were injected. *R.U.*, resonance units.

concentrations were used as positive control experiments to compare with other p47^{phox} constructs. No significant interaction with the GST-p22^{phox}Cter surface could be detected using p47^{phox}ΔCter, confirming its autoinhibited state (Fig. 2). The triple mutation S303E/S304E/S328E was sufficient to recover an affinity similar to that of p47^{phox}tandem SH3s alone: 187 nM *versus* 69 nM (supplemental Fig. S1 and supplemental Table S1). Similar results were obtained with the full-length forms of the protein; no interaction between GST-p22^{phox}Cter and p47^{phox} was observed, and the dissociation constant was determined at 55 nM for the full-length p47^{phox}TM (data not shown). The lack of affinity of wild-type p47^{phox} constructs when compared with the S303E/S304E/S328E triple mutants clearly shows the conformational change occurring during p47^{phox} activation and validates the use of p47^{phox}TM-ΔCter as a true mimic of the activated state.

Peptide Mapping—Proteolysis with acidic proteases was used to localize the differences in deuteration between the activated and autoinhibited forms of p47^{phox}. Due to ragged and nonspecific digestion, the generated peptides had to be identified by means of tandem mass spectrometry. The separate use of pepsin and protease type XIII generated 89 cleavage sites, providing a total of 127 peptides with only five occurring in both digests (supplemental Fig. S2). The combination of peptides generated by both proteases provided 99% sequence coverage. Generated peptides have an average size of 14 residues. The average number of cleavage sites and generated peptides in the AIR was twice as low (17 cleavage sites and 23 peptides per 100 residues) as in the rest of the protein where a rather good resolution was obtained (28 cleavage sites and 40 peptides per 100 residues). The polybasic nature of the AIR is most probably behind the low spatial resolution in this region. Although pepsin is known to prefer hydrophobic sites (25) and thus provided only long peptides, fungal protease XIII was shown to have preference for basic amino acids (26) and thus most probably generated very short peptides that were not detected.

Solvent Accessibility of Different p47^{phox}ΔCter Regions—The exchange kinetics of individual p47^{phox}ΔCter regions were followed on 30 peptides from the pepsin digest and 10 from the protease XIII digest, together covering 92% of the sequence. The missing 7% are due to the 4 N-terminal residues and to the gaps coming from the fact that we do not monitor exchange on the N-terminal amine of the peptides. Peptides used for DXMS study are shown in supplemental Fig. S2, and deuteration kinetics for selected peptides are shown in supplemental Fig. S3. Seven regions were determined by the difference between overlapping peptides. As an example, the deuteration percentage of region 276–279 was obtained by subtracting peptides 264–275 data from peptides 264–279 data (supplemental Fig. S4*A*). Moreover, spatial resolution was increased by the presence of short peptides. For instance, information given by peptides 161–174 was improved by the combined use of peptides 161–166 and 167–174 (supplemental Fig. S4, *B–D*).

The first information given by the local kinetics is the solvent accessibility of different p47^{phox} regions (supplemental Fig. S4*A*). As expected, the C-terminal region of p47^{phox} (residues 333–342) was quickly deuterated, as was the linker region between the PX domain and the first SH3 (residues 119–160). As shown by the protection plots (Fig. 3, *A* and *B*), these two regions are already deuterated more than 50% after only 30 s of deuterium exchange. This is in complete agreement with the predicted unfolded nature of these segments (20). It is also supported by our recent results obtained by limited proteolysis (21). Even if it seems poorly compatible with the structural and functional role that has recently been suggested for this linker (23), the latter one cannot be excluded as other structured regions show fast deuteration kinetics (*e.g.* helix 3 from PX; supplemental Fig. S4*A*). Regarding the AIR, fast deuteration kinetics are also observed, as expected from the structure, due

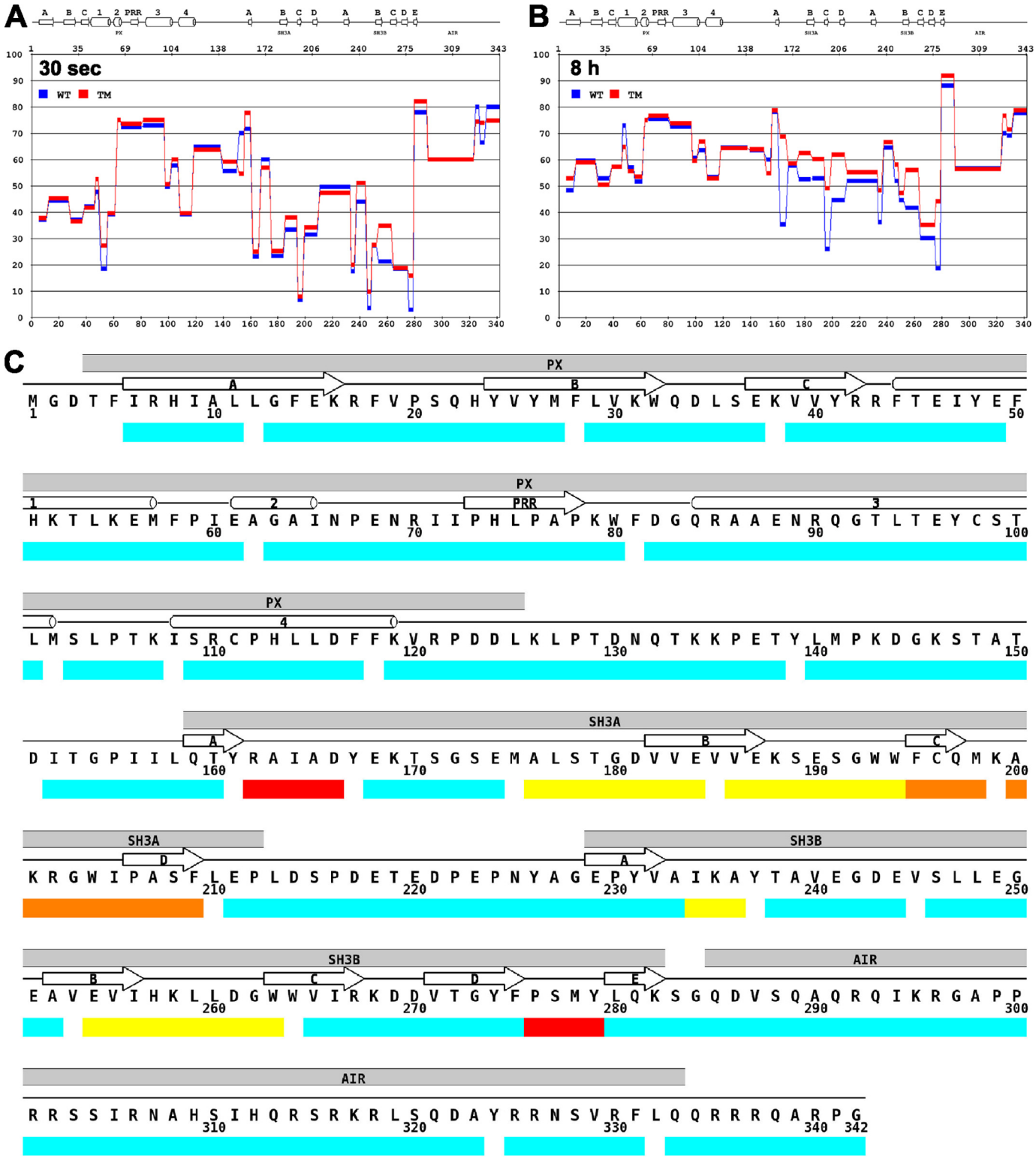

FIGURE 3. **Local kinetics of H/D exchange.** *A* and *B*, protection plots showing the deuteration levels of p47^{phox}ΔCter (*blue*) and p47^{phox}TM-ΔCter (*red*) after 30 s (*A*) and 8 h (*B*) of deuteration. *PRR*, proline-rich region. *C*, difference of deuteration between the two constructs after 8 h of deuteration: Δ%D = % of p47^{phox}TM-ΔCter − % of p47^{phox}ΔCter. *cyan*, ≤ 8%; *yellow*, ≤15%; *orange*, ≤25%, *red*, ≤35%.

to its unfolded sequence exposed at the surface of the tandem SH3s (18).

Half of the secondary structural elements described by the crystallographic and NMR results (9, 16, 18, 19, 27), such as sheets 1 and helices 1–4 from PX and sheets B-C-D from SH3A and SH3B, show slow deuteration kinetics, as expected. The other α-helices and β-sheets do not show such slow deuterium incorporation, probably because corresponding segments are covered by peptides including both unstructured and structured region (*e.g.* peptides 279–289).

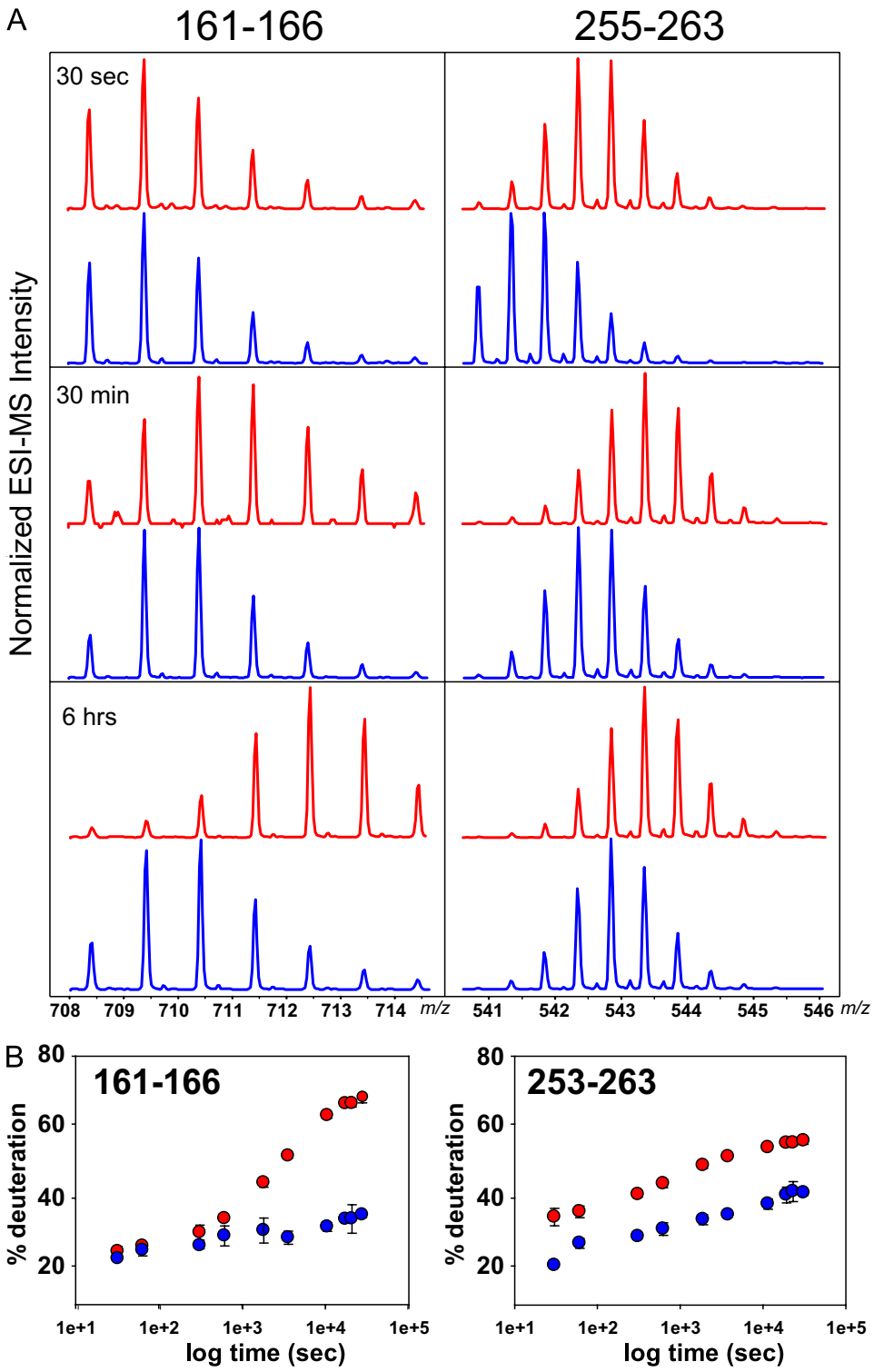

FIGURE 4. **Examples of peptides with differential kinetics of H/D exchange depending on the p47^{phox} forms.** *A*, details of isotopic profiles of two selected peptic peptides (161–166 and 255–263) from p47^{phox}ΔCter (*blue*) and p47^{phox}TM-ΔCter (*red*) demonstrating shifts toward higher masses during the deuteration. Three time points, 30 s, 30 min, and 6 h, are shown. *ESI-MS*, electrospray mass ionization-MS. *B*, deuteration kinetics of the two peptides shown in *panel A* plotted as the percentage of deuteration *versus* time for p47^{phox}ΔCter (*blue circles*) and p47^{phox}TM-ΔCter (*red circles*). Values are the average of two independent experiments.

Deuterium Exchange Comparison between Autoinhibited and Activated Forms, Identification of Unmasked Surfaces upon Activation—Structural changes occurring upon p47^{phox} activation are best evidenced by examining the differences between p47^{phox}TM-ΔCter and p47^{phox}ΔCter deuteration percentages (Fig. 3*C*). Actually, upon deuterium incorporation, the isotopic distributions of the peptides are shifted to the higher masses, and for some peptides, such as 161–166 or 255–263 (Fig. 4), the incorporation is faster for p47^{phox}TM-ΔCter than for p47^{phox}ΔCter. This faster deuterium incorporation for p47^{phox}TM-ΔCter can be directly interpreted as better accessibility to the solvent following conformational changes. Five regions, all located within the tandem SH3s, showed increased deuteration rates for p47^{phox}TM-ΔCter, whereas no significant differences were highlighted in the PX domain. Deuteration differences between both autoinhibited and activated forms of p47^{phox} were plotted onto the available structures of the "tandem SH3s-AIR supercomplex" and of the PX domain (Fig. 5*A*) (18). When looking at the tandem SH3s, two different events can be distinguished to interpret the observed unmasked surfaces in the activated form.

The first one corresponds to peptides encompassing residues 186–194 from SH3A and 254–263 from SH3B. These two regions, facing each other, are the two Src loops that are known to be exposed to the solvent after activation to bind the p22^{phox}Cter part (13, 14, 24, 28–31). Two other regions within SH3B (234–236 and 276–279) are protected in the autoinhibited state and form an inner surface masked by the AIR. In all these regions, the better accessibility to the solvent upon activation can be explained by the release of the AIR, as illustrated in Fig. 5, *B* and *C*.

Secondly, another surface exposed upon p47^{phox} activation was detected by DXMS (residues 162–166, 176–185, and 195–209). This region encompasses the whole SH3A lateral surface (Fig. 5, *D* and *E*), which has never been suggested to be involved in the activation process. In a recent study of the p47^{phox} resting state, crystallographic structures of the PX domain and tandem SH3s (16, 18) have been fitted in the low resolution envelopes of the whole protein obtained by small

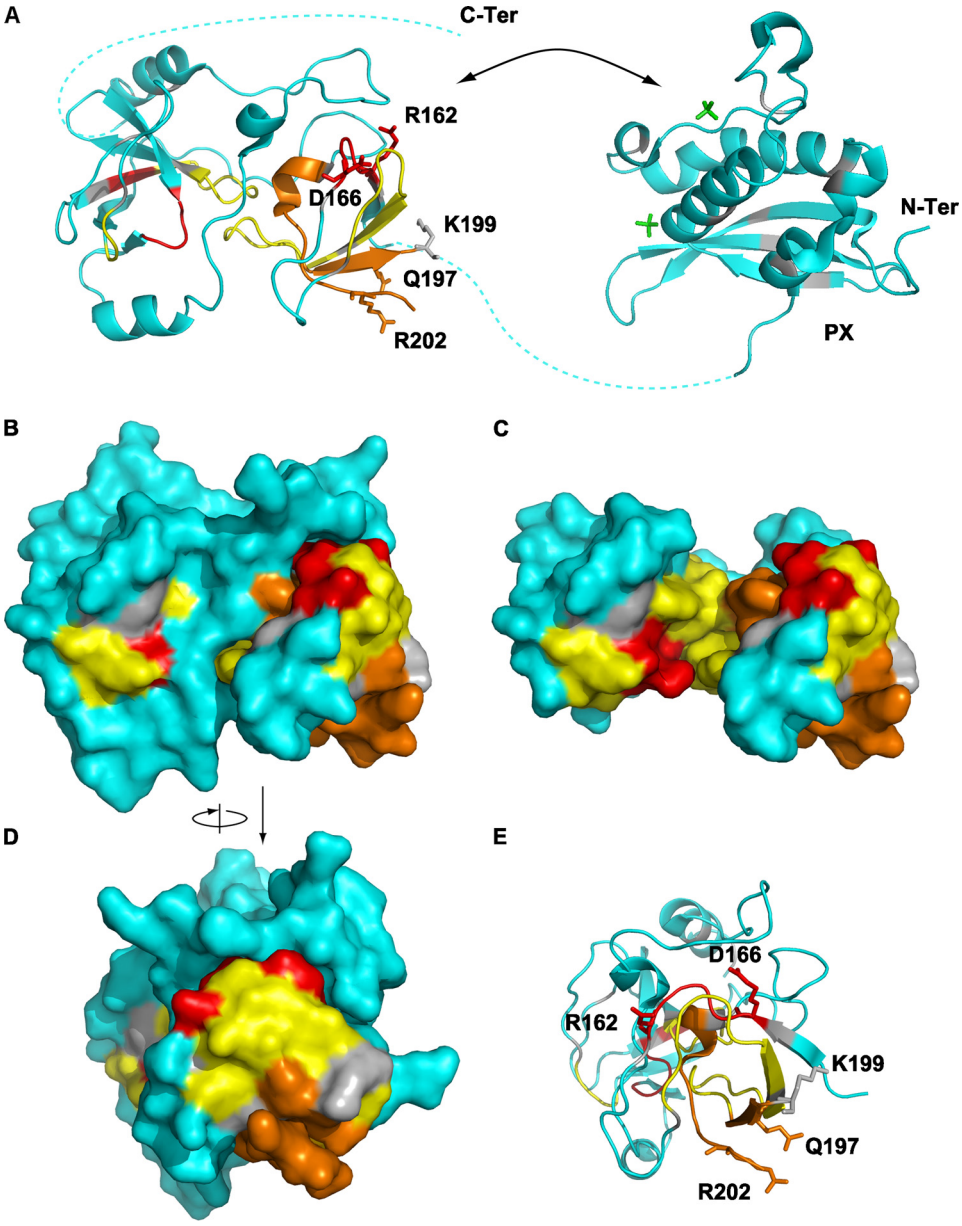

FIGURE 5. **Local kinetics of H/D exchange transferred onto the crystallographic structures of the autoinhibited SH3 tandem (PDB: 1NG2) (18) and PX domain (PDB: 1O7K) (16).** Difference of deuteration between the two constructs after 8 h of deuteration: Δ%D = % of p47^{phox}TM-ΔCter − % of p47^{phox}ΔCter. *cyan*, ≤8%; *yellow*, ≤15%; *orange*, ≤25%; *red*, ≤ 35%. *A*, PX domain and tandem SH3s-AIR supercomplex structures correspond to residues 1–123 and 157–332 of p47^{phox}, respectively. Undetermined structures of flexible regions are represented as *dashed lines*, and mutated residues are represented as *sticks*. The sulfates bound in the phospholipid-binding sites are shown in *stick representation* (*green*). *B* and *C*, the surface of the autoinhibited tandem SH3s is represented with (*B*) or without (*C*) the AIR, mimicking the resting and activated states, respectively. *D* and *E*, lateral view of the autoinhibited tandem SH3s showing the highlighted region as a *surface* (*D*) or as *sticks* (*E*).

angle x-ray scattering (20). From the derived domain arrangement, the surface identified here is potentially localized in close vicinity of the PX domain in the autoinhibited state. The unmasking of these regions coupled with the enhancement of lipid binding properties strongly support our initial proposal that the SH3A lateral surface is involved in the PX domain locking in the resting state (Fig. 5*A*, *arrow*).

We expected to see a deuteration difference within the PX domain and the AIR because previous work clearly showed that the PX domain and AIR release upon activation (21). The absence of difference in the PX can be explained by differences located for the most part at the protein surface that cannot be detected by DXMS as lateral chain hydrogens are not monitored.

R162A/D166A Mutations in the SH3A Lateral Surface Induce the PX Domain Release—To confirm the direct interaction between the SH3A and the PX domain through the surface highlighted by DXMS, a mutagenesis study was conducted. Some of the residues exposed to the solvent, potentially responsible for this interaction (Fig. 5, *A* and *E*), were chosen. The following single and double mutations were made: R162A, D166A, R162A/D166A, Q197A, K199E, and R202A. Binding to the C-terminal part of p22^{phox} was tested for each mutant using SPR analysis. In contrary to the tandem SH3s, none of these mutants were able to interact with p22^{phox} (Fig. 6, *A* and *B*, and data not shown). This proves that the tandem SH3s-AIR supercomplex is not disrupted in mutants of this lateral surface.

Release of the PX domain for each mutant was determined by pull-down assay with liposomes, as described previously (21). Of the tested mutants, only R162A/D166A showed drastically enhanced binding properties with specific phospholipids PtdIns(3,4)P_2 when compared with p47^{phox}ΔCter (Fig. 6*C*). The structural integrity of p47^{phox}ΔCter, p47^{phox}TM-ΔCter, and p47^{phox}R162A/D166A-ΔCter was confirmed by circular dichroism (Fig. 6*D*). These data suggest a specific role of residues Arg-162 and Asp-166 in PX domain inhibition. To highlight the importance of both residues in the maintenance of the p47^{phox} autoinhibited state, the global kinetics of deuteration were determined, as described previously (21). The p47^{phox}R162A/D166A-ΔCter deuteration rate is in between the rates of p47^{phox}ΔCter and p47^{phox}TM-ΔCter (Fig. 6*E*). This result reflects an intermediate conformation of this mutant that has never been described. Indeed, it possesses a closed tandem SH3s-AIR supercomplex with an open PX domain accessible for lipid binding.

DISCUSSION

The molecular activation of the NOX2-based NADPH oxidase has been the subject of intense studies over the last few

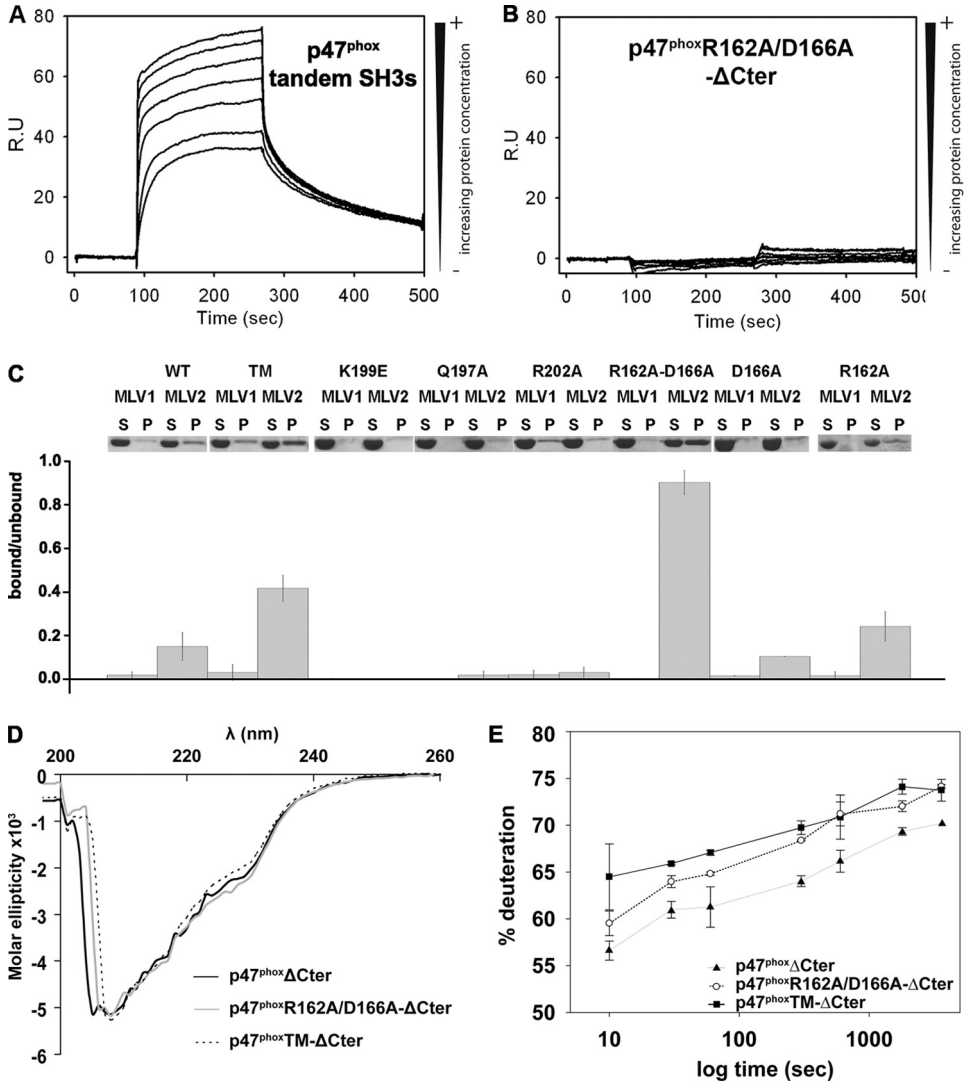

FIGURE 6. **R161A/D166A mutations induce selective opening of the PX domain.** *A* and *B*, surface plasmon resonance results obtained for p47^{phox}tandem SH3s (*A*) and p47^{phox}R162A/D166A-ΔCter (*B*) on CM4 chips functionalized with GST-p22^{phox}Cter. Increasing concentrations (from 40 nM to 2.56 μM) of each construct were injected. *R.U.*, resonance units. *C*, phosphoinositide binding activity of p47^{phox}ΔCter, p47^{phox}TM-ΔCter, p47^{phox}K199E-ΔCter, p47^{phox}Q197A-ΔCter, p47^{phox}R202A-ΔCter, p47^{phox}R162A/D166A-ΔCter, p47^{phox}R162A-ΔCter, and p47^{phox}D166A-ΔCter. All proteins were incubated with liposomes containing POPC:POPE 50:50 (MLV1) or POPC:POPE:POPA:PtdIns(3,4)P_2 45:45:5:5 (MLV2). *S* and *P* are liposomal supernatant and pellet after centrifugation, corresponding to the unbound and bound fraction, respectively. Samples were analyzed by SDS-PAGE and quantified by densitometry. *Error bars* indicate S.E. *D*, circular dichroism of p47^{phox}ΔCter, p47^{phox}R162A/D166A-ΔCter, and p47^{phox}S303/304/328E-ΔCter. *E*, deuteration kinetics for p47^{phox}ΔCter (*black triangles*, *gray line*), p47^{phox}TM-ΔCter (*black squares*), and p47^{phox}R162A/D166A-ΔCter (*open circles*, *dashed line*) at pD 7.4.

decades. Considering the level of reactive oxygen species potentially produced by this specialized system, tight regulation is of primary importance. Indeed, an abnormal increase in this activity can lead to dramatic consequences, as observed in neurodegenerative pathologies (such as Alzheimer disease, Parkinson disease, HIV dementia, and demyelinating disease) (2). Therefore, better knowledge of the molecular mechanism behind this tightly regulated system is highly important, not only for basic knowledge but also to advance toward therapeutic strategies for better control of these pathological deregulations.

Two main events are central in the activation of NADPH oxidase. Flavocytochrome b_{558} requires direct interaction with Rac1/2 and p67^{phox} to trigger the electron transfer (32, 33). The presence of p67^{phox} at the membrane requires conformational changes of p47^{phox} that will orchestrate their co-translocation from the cytosol. Despite the crucial role played by these two activation steps, the related molecular mechanisms are poorly understood. Our study brings new insights into the structural changes undergone by p47^{phox} upon activation.

Interaction of Activated p47^{phox} with p22^{phox}—It was shown that p47^{phox}TM-ΔCter lipid binding properties are enhanced in contrast to p47^{phox}ΔCter (21). However, its capacity to interact with p22^{phox} remained to be confirmed. The interaction properties of the autoinhibited (p47^{phox}ΔCter) and activated state mimic (p47^{phox}TM-ΔCter) with GST-p22^{phox}Cter have thus been addressed by SPR. As expected, p47^{phox}ΔCter did not interact, whereas p47^{phox}TM-ΔCter showed interaction properties that were similar to the p47^{phox}tandem SH3s (positive control, Fig. 2). The interaction between p47^{phox} and the C-terminal region of p22^{phox} has already been effectively described from the biochemical (13, 18, 24, 28, 30, 31) and structural (14, 29) points of view.

Concerning tandem SH3s, the dissociation constant relative to this interaction using isothermal titration calorimetry (18) and fluorescence titration methods (18, 29) led to K_d values of 0.19, 0.40, and 0.64 μM, respectively. As for full-length p47^{phox}TM, a higher K_d value was determined by fluorescence titration at 17.8 μM (18). These affinities are lower than the affinity reported here, with a K_d estimated at 69 nM for the tandem SH3s and 187 nM for the p47^{phox}TM-ΔCter. This difference might be attributed to the use of a p22^{phox} C terminus, which is three times longer (63 residues *versus* 20) than reported in previous studies. The C terminus of p22^{phox} used in this study corresponds to the entire cytosolic region following the last putative transmembrane segment. The improvement in affinity suggests that the additional residues, apart from the canonical proline-rich region, may also play a role in stabilizing the p47^{phox}/p22^{phox} interaction. However, the affinity obtained with different analytical methods, p47^{phox} constructs, and p22^{phox}Cter peptides of various lengths may only be compared

with great caution. The most important information here is the ability to discriminate between open and closed tandem SH3s, reflecting the activated or the autoinhibited states of the protein.

Deciphering the Molecular Opening of p47^{phox}—The DXMS local kinetics presented here are a natural follow-up to our first study of the conformational changes occurring upon p47^{phox} activation (21). Here we precisely localized unmasked regions during AIR and PX release. Indeed, the bottom of the tandem SH3s groove, including the Src loops extending from both SH3s, becomes accessible. This is a definitive structural demonstration that the addition of targeted negative charges induces AIR release (by mutation here and phosphorylation *in vivo*). At this point, p47^{phox} is now able to progress further to the next step along the activation process: the interaction with p22^{phox}.

The existence of a "dormant" state of p47^{phox}, involving region unmasking upon activation, was proposed 16 years ago (13). Since then, the two SH3s domains and the N-terminal region of the protein (designated as the PX domain in 1996) have been pointed out in this mechanism (34, 35). The PX domain lipid binding property was identified in 2001 (10), and its enhancement in the activated form clearly established 2 years later (8). Over this long period, the PX domain was believed to interact internally with SH3B (4, 7, 8, 16, 24, 30). The structure of the tandem SH3s-AIR supercomplex raised doubts about this interaction (17–19). Finally, small angle x-ray scattering molecular envelopes of the entire p47^{phox} instead suggested that SH3A was the internal PX target (20). Our present study reveals the unmasking of a new surface on the lateral side of SH3A. This enhanced accessibility and the higher lipid binding property of the activated state (Fig. 6*C*) strongly support the proposal that this lateral surface can be involved in PX interaction.

Identification of Residues Involved in PX-SH3A Interaction by Site-directed Mutagenesis—To more precisely identify the residues that are directly involved in PX binding, five mutants were created within the new surface identified by DXMS. None of them showed interaction with the p22^{phox}Cter part (Fig. 6, *A* and *B*, and data not shown), confirming tandem SH3s-AIR supercomplex integrity. However, the double mutant p47^{phox}R162A/D166A-ΔCter was able to interact with specific phospholipids (Fig. 6*C*), reflecting PX domain release. The single mutants R162A and D166A do not show such enhancement in lipid binding (Fig. 6*C*), showing a synergistic effect of both residues in PX domain locking. Interestingly, the 2 residues identified are located within peptides 161–166, which show the largest deuteration difference between p47^{phox}ΔCter and p47^{phox}TM-ΔCter in DXMS local kinetics (Fig. 4*B*). This suggests that these residues play a role in the p47^{phox} autoinhibition mechanism. This semi-open conformation is further supported by DXMS global kinetics showing an intermediate surface accessibility between the inhibited and activated states for p47^{phox}R162A/D166A-ΔCter.

A recent study pointed out that the region upstream from the SH3A module (residues 151–158) could be involved in the lipid-binding site inhibition, as shown by the PX domain opening upon substitution by a polyglycine linker (23). Another study showed that residues Ile-152 and Thr-153 are crucial for Nox2 activation (36) but do not affect p47^{phox} translocation properties in response to phorbol myristate acetate addition. These two studies underline a role for this stretch of amino acids localized close to the surface highlighted here by DXMS. However, this stretch is already fully deuterated after 30 s, and no deuteration difference can be seen between p47^{phox} activated and autoinhibited forms (Fig. 3*C*). These DXMS data firstly prove that this 151–158 region is readily accessible. Secondly, the absence of deuteration difference between both states does not allow conferring on this region any structural role in p47^{phox} activation. It may be involved at a later stage, after oxidase assembly, as suggested by Taura *et al.* (36).

Intramolecular Signal Transduction within p47^{phox} upon Activation, Coupling between AIR Release and PX Opening—Apart from identifying the PX docking site on SH3A, an even more important pursuit is understanding the domino effect explaining how phosphorylations occurring in the p47^{phox} C-terminal part make the PtdIns(3,4)P_2-binding site accessible, three modules upstream along the protein. Among the different mutants studied here, the properties of the double mutant R162A/D166A address this question.

When looking closer at the tandem SH3s-AIR supercomplex structure (18, 19), residue Arg-162 from SH3A appears to be directly connected to the AIR (Fig. 7*A*). Arg-162 is at the center of a hydrogen-bond network connecting the SH3A surface with the AIR in its bound state (Fig. 7*B*). It interacts directly with His-309 and indirectly with Ser-310 through stabilization of residue Glu-211. From this core network around Arg-162, additional residues Ile-164 and Pro-212 from the SH3A and Ile-311 and His-312 from the AIR are involved in additional contact within this interface (Fig. 7*B*).

In contrast, no interaction of residue Asp-166 with the AIR can be stated from the available crystal structures (Protein Data Bank (PDB) 1NG2 and 1UEC). Therefore, the synergistic effect observed in the double mutant can be explained by a combined stabilization of the PX domain by residues Arg-162 and Asp-166. Mutations of these residues lead to PX domain release without affecting tandem SH3s-AIR supercomplex integrity, but AIR release (such as in p47^{phox}TM-ΔCter) also leads to PX domain release.

The coupling between AIR and the PX domain can be assigned to Arg-162. Upon AIR release, triggered by serine phosphorylations, disruption of the hydrogen-bond network around Arg-162 will disorganize the side chain structural organization of the highlighted peptides 162–166. This could be sensed by the PX domain docked on this lateral surface and would finally trigger its release (Fig. 7*C*). As already mentioned by our group (21) and others (8, 16, 23), although not activated, p47^{phox}ΔCter shows a basal interaction with lipids in pulldown experiments (Fig. 6*C*). This reflects an equilibrium between the two different PX conformations, closed and open. In the case of p47^{phox}TM-ΔCter, because the AIR is released, the PX docking site is destabilized, particularly around residue Arg-162, allowing a displacement of this equilibrium that favors the open form, *i.e.* the lipid-bound form. In light of the results presented here, we can assume that in the case of p47^{phox}R162A/D166A-ΔCter, the PX is not only released but also unable to interact

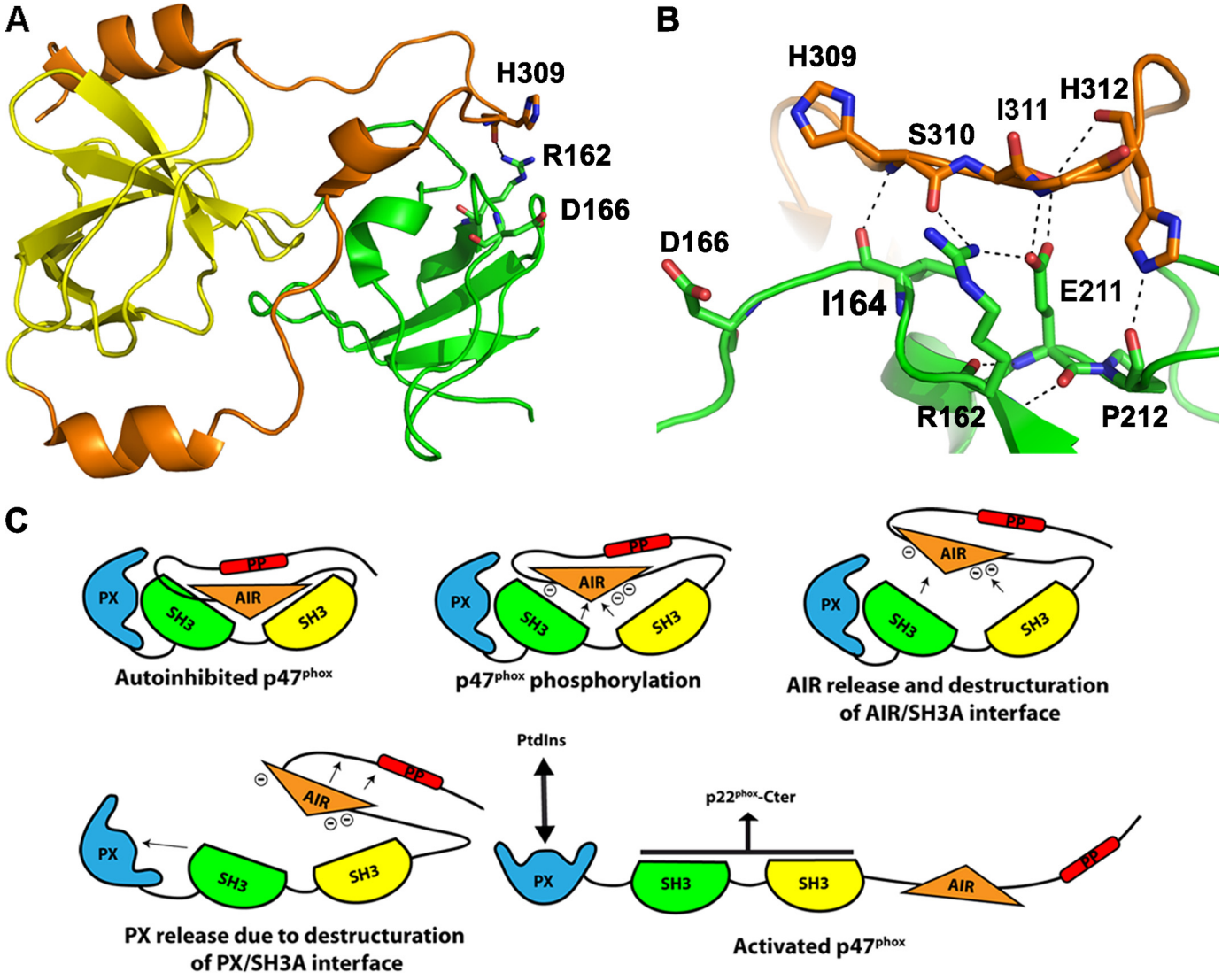

FIGURE 7. **Molecular mechanism of PX release upon AIR phosphorylation.** *A*, structure of the tandem SH3s inhibited by the AIR (PDB: 1NG2) (18). SH3A, SH3B, and AIR are represented in green, yellow, and orange, respectively. Residues Arg-162, Asp-166, and His-309 are shown as *sticks*. *B*, close-up showing the network of polar interactions between residues Arg-162, Ile-164, Glu-211, and Pro-212 from SH3A (*green*) and residues His-309, Ser-310, Ile-311, and His-312 from AIR (*orange*). *C*, schematic representation of p47^{phox} activation mechanism showing how phosphorylation of the AIR leads to the PX domain release through the surface identified in this study.

with the lateral surface of SH3A due to disappearance of these crucial docking residues. In this mutant, the equilibrium is totally displaced toward the open form of the PX. This explains the much higher interaction with lipids observed for p47^{phox}R162A/D166A-ΔCter than for p47^{phox} TM-ΔCter (Fig. 6*C*).

A more systematic site-directed mutagenesis study must be conducted on both regions encompassing residues 306–312 from the AIR and this newly identified surface from SH3A to describe this mechanism more accurately. Mutations in the PX domain could also lead to the identification of the residues involved in the interaction with this SH3A lateral surface.

For many years, researchers have been trying to explain how the phosphorylation of at least 3 serine residues on one part of p47^{phox} leads to the PX domain release. Here a surface involved in PX autoinhibition has finally been localized on SH3A. Moreover, 2 residues from this region are pointed out as playing a key role in the intramolecular signal transduction from the AIR to the PX domain. The emerging mechanism deciphered here in p47^{phox} to control a global assembly process in response to phosphorylations has never been reported before. To our knowledge, it is a unique structural organization enabling an internal signal transduction along four distinct modules.

Acknowledgments—We thank Daniel Kavan for developing the scripts, thus facilitating data processing and interpretation. We also thank Patrice Vachette and Dominique Durand for careful reading of the manuscript and fruitful scientific discussions.

REFERENCES

1. Sumimoto, H. (2008) *FEBS J.* **275,** 3249–3277
2. Bedard, K., and Krause, K. H. (2007) *Physiol. Rev.* **87,** 245–313
3. Segal, A. W. (1996) *Mol. Med. Today* **2,** 129–135
4. Lapouge, K., Smith, S. J., Groemping, Y., and Rittinger, K. (2002) *J. Biol. Chem.* **277,** 10121–10128
5. Nakamura, R., Sumimoto, H., Mizuki, K., Hata, K., Ago, T., Kitajima, S.,

Takeshige, K., Sakaki, Y., and Ito, T. (1998) *Eur. J. Biochem.* **251,** 583–589
6. Noda, Y., Kohjima, M., Izaki, T., Ota, K., Yoshinaga, S., Inagaki, F., Ito, T., and Sumimoto, H. (2003) *J. Biol. Chem.* **278,** 43516–43524
7. Massenet, C., Chenavas, S., Cohen-Addad, C., Dagher, M. C., Brandolin, G., Pebay-Peyroula, E., and Fieschi, F. (2005) *J. Biol. Chem.* **280,** 13752–13761
8. Ago, T., Kuribayashi, F., Hiroaki, H., Takeya, R., Ito, T., Kohda, D., and Sumimoto, H. (2003) *Proc. Natl. Acad. Sci. U.S.A.* **100,** 4474–4479
9. Hiroaki, H., Ago, T., Ito, T., Sumimoto, H., and Kohda, D. (2001) *Nat. Struct. Biol.* **8,** 526–530
10. Kanai, F., Liu, H., Field, S. J., Akbary, H., Matsuo, T., Brown, G. E., Cantley, L. C., and Yaffe, M. B. (2001) *Nat. Cell Biol.* **3,** 675–678
11. Stahelin, R. V., Burian, A., Bruzik, K. S., Murray, D., and Cho, W. (2003) *J. Biol. Chem.* **278,** 14469–14479
12. Zhan, Y., Virbasius, J. V., Song, X., Pomerleau, D. P., and Zhou, G. W. (2002) *J. Biol. Chem.* **277,** 4512–4518
13. Sumimoto, H., Kage, Y., Nunoi, H., Sasaki, H., Nose, T., Fukumaki, Y., Ohno, M., Minakami, S., and Takeshige, K. (1994) *Proc. Natl. Acad. Sci. U.S.A.* **91,** 5345–5349
14. Taylor, R. M., Lord, C. I., Riesselman, M. H., Gripentrog, J. M., Leto, T. L., McPhail, L. C., Berdichevsky, Y., Pick, E., and Jesaitis, A. J. (2007) *Biochemistry* **46,** 14291–14304
15. Wilson, L., Butcher, C., Finan, P., and Kellie, S. (1997) *Inflamm. Res.* **46,** 265–271
16. Karathanassis, D., Stahelin, R. V., Bravo, J., Perisic, O., Pacold, C. M., Cho, W., and Williams, R. L. (2002) *EMBO J.* **21,** 5057–5068
17. Nauseef, W. M. (2004) *Histochem. Cell Biol.* **122,** 277–291
18. Groemping, Y., Lapouge, K., Smerdon, S. J., and Rittinger, K. (2003) *Cell* **113,** 343–355
19. Yuzawa, S., Suzuki, N. N., Fujioka, Y., Ogura, K., Sumimoto, H., and Inagaki, F. (2004) *Genes Cells* **9,** 443–456
20. Durand, D., Cannella, D., Dubosclard, V., Pebay-Peyroula, E., Vachette, P., and Fieschi, F. (2006) *Biochemistry* **45,** 7185–7193
21. Marcoux, J., Man, P., Castellan, M., Vivès, C., Forest, E., and Fieschi, F. (2009) *FEBS Lett.* **583,** 835–840
22. Zhang, Z., and Marshall, A. G. (1998) *J. Am. Soc. Mass Spectrom.* **9,** 225–233
23. Shen, K., Sergeant, S., Hantgan, R. R., McPhail, L. C., and Horita, D. A. (2008) *Biochemistry* **47,** 8855–8865
24. Ago, T., Nunoi, H., Ito, T., and Sumimoto, H. (1999) *J. Biol. Chem.* **274,** 33644–33653
25. Tang, J. (1963) *Nature* **199,** 1094–1095
26. Zhang, H. M., Kazazic, S., Schaub, T. M., Tipton, J. D., Emmett, M. R., and Marshall, A. G. (2008) *Anal. Chem.* **80,** 9034–9041
27. Yuzawa, S., Ogura, K., Horiuchi, M., Suzuki, N. N., Fujioka, Y., Kataoka, M., Sumimoto, H., and Inagaki, F. (2004) *J. Biol. Chem.* **279,** 29752–29760
28. Nobuhisa, I., Takeya, R., Ogura, K., Ueno, N., Kohda, D., Inagaki, F., and Sumimoto, H. (2006) *Biochem. J.* **396,** 183–192
29. Ogura, K., Nobuhisa, I., Yuzawa, S., Takeya, R., Torikai, S., Saikawa, K., Sumimoto, H., and Inagaki, F. (2006) *J. Biol. Chem.* **281,** 3660–3668
30. Shiose, A., and Sumimoto, H. (2000) *J. Biol. Chem.* **275,** 13793–13801
31. Sumimoto, H., Hata, K., Mizuki, K., Ito, T., Kage, Y., Sakaki, Y., Fukumaki, Y., Nakamura, M., and Takeshige, K. (1996) *J. Biol. Chem.* **271,** 22152–22158
32. Gorzalczany, Y., Sigal, N., Itan, M., Lotan, O., and Pick, E. (2000) *J. Biol. Chem.* **275,** 40073–40081
33. Li, X. J., Fieschi, F., Paclet, M. H., Grunwald, D., Campion, Y., Gaudin, P., Morel, F., and Stasia, M. J. (2007) *J. Leukoc. Biol.* **81,** 238–249
34. Leto, T. L., Adams, A. G., and de Mendez, I. (1994) *Proc. Natl. Acad. Sci. U.S.A.* **91,** 10650–10654
35. Ponting, C. P. (1996) *Protein Sci.* **5,** 2353–2357
36. Taura, M., Miyano, K., Minakami, R., Kamakura, S., Takeya, R., and Sumimoto, H. (2009) *Biochem. J.* **419,** 329–338